fluids

MDPI

Article

Hydraulic Characterization of a Direct-Acting Pressure-Reducing Valve Using CFD and Experimental Validation

Gonzalo López-Villacís [1,*], Pablo Valle-Velasco [1], Martha Sevilla-Abarca [2], Diana Peralta-Zurita [3] and Segundo Espín-Lagos [1]

[1] Facultad de Ingeniería Civil y Mecánica, Universidad Técnica de Ambato, Ambato 180329, Ecuador; prvalle@uta.edu.ec (P.V.-V.); sespin@uta.edu.ec (S.E.-L.)
[2] Facultad de Ingeniería en Sistemas, Electrónica e Industrial, Universidad Técnica de Ambato, Ambato 180329, Ecuador; marthaesevilla@uta.edu.ec
[3] Facultad de Arquitectura e Ingenierías, Universidad Internacional SEK, Quito 170304, Ecuador; diana.peralta@uisek.edu.ec
* Correspondence: gelopez@uta.edu.ec; Tel.: +593-98-376-055

Abstract

This study presents the hydraulic characterization of a direct-acting pressure-reducing valve (PRV) using a combined experimental and numerical approach. An experimental test bench was implemented to measure inlet, control port, and outlet pressures over a flow rate range from 0 to 4.0 m^3/h, under a constant inlet pressure of 8 bar and a set pressure of 3 bar. In parallel, a three-dimensional steady-state CFD model was developed using a sequential force balance analysis between hydraulic and spring restoring forces. The results show good agreement between numerical predictions and experimental data, with a maximum error below 10% in outlet pressure. The pressure drop exhibited a nonlinear increasing trend with flow rate, reaching values close to 1.8 bar at 4.0 m^3/h. The flow coefficient K_v remained within a range of 2.2–3.0, while the pressure regulation coefficient S remained below 0.05, indicating stable regulation performance. Additional simulations at 25 bar provided improved agreement with manufacturer data, suggesting that catalog curves may be based on nominal pressure conditions. The proposed methodology demonstrates that steady-state CFD coupled with force balance analysis is an effective and computationally efficient approach for predicting the hydraulic behavior of direct-acting PRVs.

Keywords: pressure-reducing valve; computational fluid dynamics; experimental validation; pressure drop; pressure regulation; force balance

Academic Editor: Antonio F. Miguel

Received: 24 April 2026
Revised: 20 May 2026
Accepted: 26 May 2026
Published: 2 June 2026

1. Introduction

Pressure control in water supply systems is essential to ensure the safe and efficient operation of installations, as well as to extend the service life of pipes, fittings, and end-use equipment. In small-scale residential and commercial networks, overpressures and pressure fluctuations are common, increasing the risk of leaks, premature failures, and unstable operating conditions, particularly in the presence of topographical variations or high supply pressures [1–4]. In this context, direct-acting pressure-reducing valves (PRVs) are widely used as regulating devices to maintain downstream pressure within acceptable limits.

The hydraulic performance of a PRV is not governed by a single factor but by the interaction between its internal geometry, the regulating mechanism, and the flow conditions. This interaction determines both the pressure distribution and pressure losses, as well as

the system response to variations in flow rate. Although these devices are designed and tested according to international standards such as EN 1567 [1] and ISO 10522 [5], the performance curves provided by manufacturers correspond to specific laboratory conditions. Consequently, their application in real systems requires assessing the extent to which these curves represent the actual behavior of the device under different operating conditions, which justifies the use of complementary experimental and numerical approaches [6,7].

In this regard, computational fluid dynamics (CFD) has proven to be a particularly useful tool for the analysis of internal flows in complex geometries. Its application enables detailed characterization of pressure fields, velocity distributions, and turbulent structures, which are difficult to obtain through experimental measurements alone [8,9]. In the field of control valves, several studies have applied CFD to investigate pressure losses, flow-induced forces, cavitation phenomena, and the influence of geometry on hydraulic performance [10–16]. However, most of these studies focus on industrial valves or different configurations, while direct-acting PRVs used in residential systems have received comparatively less attention, particularly from a combined experimental–numerical perspective [6,7,15].

A relevant characteristic of this type of valve is that the outlet pressure is not determined solely by hydraulic restriction, but also by the balance between the force exerted by the flow on the moving element and the spring restoring force of the regulating mechanism. This coupling between fluid behavior and the mechanical system can be analyzed using different numerical approaches depending on the desired level of complexity and computational cost. From a practical standpoint, however, it is of interest to explore simpler methodologies capable of describing the system behavior using steady-state simulations, provided that physical consistency and predictive capability are preserved [12–16].

Despite advances in the analysis of control valves, there is still limited hydraulic characterization of direct-acting pressure-reducing valves used in residential applications based on integrated experimental–numerical approaches. This limitation becomes particularly relevant in practical applications, where the selection and operation of these devices often rely on manufacturer catalog data [17], without independent verification under representative operating conditions.

In this context, the objective of this study is to perform the hydraulic characterization of a direct-acting pressure-reducing valve using a combined experimental and numerical approach. To this end, a hydraulic test bench is implemented and a three-dimensional steady-state CFD model is developed, based on a sequential force equilibrium procedure between hydraulic and spring restoring forces, using a simplified steady-state CFD approach coupled with a sequential force balance analysis. The main contribution of this work lies in evaluating the capability of this simplified approach to reproduce pressure-drop curves and the regulation behavior of the valve over a representative range of flow rates, as well as in its experimental validation and comparison with manufacturer data [17].

Recent studies have emphasized the importance of properly characterizing the flow regime and selecting appropriate turbulence modeling approaches for internal turbulent flows and throttling devices [18,19]. The Reynolds number remains a fundamental parameter for identifying flow conditions and supporting the applicability of turbulence models in hydraulic systems [18]. In addition, recent analyses of turbulence simulation strategies have highlighted the limitations of conventional RANS-based approaches when dealing with separated and recirculating flows [19]. These aspects are particularly relevant in pressure-reducing valves, where strong pressure gradients and localized acceleration occur in the throttling region [20].

2. Materials and Methods

2.1. General Approach

The hydraulic characterization of the pressure-reducing valve (PRV) was carried out using a combined experimental–numerical approach, with the aim of analyzing its behavior in terms of pressure, flow rate, and pressure drop under controlled conditions. This type of approach allows for experimental measurements to be complemented with detailed information on the flow field obtained through CFD simulations, which is particularly useful in systems with complex internal geometries [8,9,13].

The methodological procedure was structured into two main stages. In the first stage, experimental tests were conducted using a hydraulic test bench to obtain pressure and flow-rate data. In the second stage, three-dimensional steady-state numerical simulations were performed to reproduce the behavior of the valve through a model based on force equilibrium. The integration of both stages made it possible to validate the numerical model and to evaluate its ability to reproduce the performance curves reported by the manufacturer.

2.2. Valve Selection

A representative pressure-reducing valve (PRV) commonly used in residential water supply systems was selected. It is a direct-acting, piston-based valve with a nominal diameter of DN15 (1/2″), widely used in domestic installations due to its simple design, low cost, and ease of installation.

The valve analyzed is of European origin and is manufactured by Genebre (Spain), complying with the EN 1567 standard for pressure-reducing valves in potable water systems [1]. Its selection was based both on its availability in the local market and on the fact that its operating characteristics are representative of devices used in real applications.

The main technical specifications provided by the manufacturer [17,21] are summarized in Table 1.

Table 1. Technical specifications of the pressure-reducing valve.

Parameter	Specification
Brand	GENEBRE
Origin	Spain
Model/Series	Redux GE
Reference Code	3318 04
Nominal Diameter	DN15 (1/2″)
Nominal Pressure	25 bar (PN25)
Body Material	CW617N brass
Regulation Range	1.0–5.5 bar
Maximum Temperature	130 °C
Reference Standard	EN 1567

Figure 1 shows the valve in its physical configuration and the three-dimensional model used for CFD simulations. These devices have a defined flow direction, indicated by an arrow on the body, which must be respected to ensure proper operation.

According to the manufacturer's catalog, the spring is made of EN 10270-1 SH steel. Accordingly, the shear modulus of the material was assumed to be G = 79,300 MPa, a value representative of steels used in helical springs and consistent with ranges reported in the literature [22].

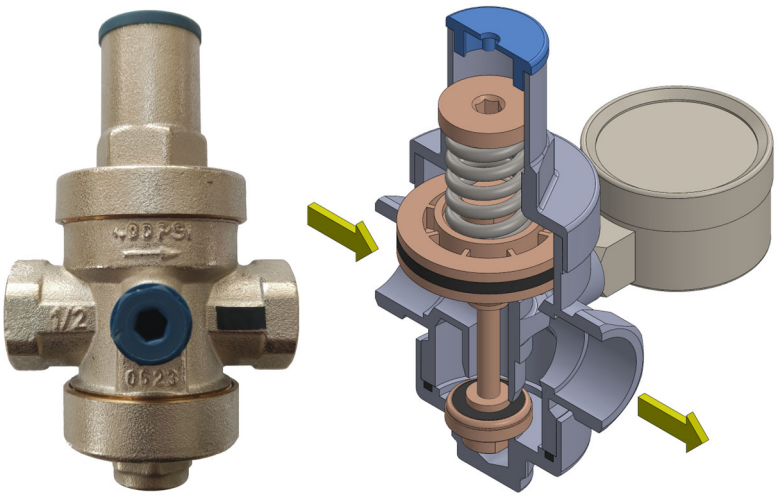

(**a**) (**b**)

Figure 1. Pressure-reducing valve (PRV): (**a**) physical configuration; (**b**) three-dimensional model used for CFD simulations.

The spring analyzed has the following geometric parameters: wire diameter d = 3 mm, mean diameter D = 15.8 mm, and number of active coils N = 4.5. Spring stiffness was determined using the classical expression for helical springs:

$$k = \frac{d^4 G}{8D^3 N} \tag{1}$$

yielding a value of k = 45.24 N/mm.

To estimate the regulation limits of the valve, the maximum spring deflection $x_{\max}$ was determined from the difference between the free length L_0 = 36 mm and the solid length L_s, calculated as follows:

$$L_s = dN_t \tag{2}$$

where $N_t = N + 2$ corresponds to the total number of coils. In this way, L_s = 19.5 mm is obtained, and therefore $x_{\max}$ = 16.5 mm.

The maximum spring restoring force was determined using Hooke's law:

$$F_R = kx \tag{3}$$

resulting in a maximum force of $F_{R,\max}$ = 746.46 N.

2.3. Experimental Setup

The hydraulic test bench was designed with the aim of minimizing parasitic head losses and flow disturbances not associated with the valve under study. To achieve this, the number of fittings was reduced, and pipe diameters were selected to promote stable flow conditions.

The system was instrumented with three analog pressure gauges with an accuracy class of 0.5% for pressure measurement and an ultrasonic flowmeter for volumetric flow-rate recording. In the test section, 1/2-inch piping was used, corresponding to the nominal diameter of the valve, while 1-inch piping was employed in the upstream and downstream sections in order to reduce distributed head losses.

At the system outlet, a 3 m long straight pipe section (1-inch diameter) was installed to promote flow stabilization prior to discharge. Additionally, stabilization lengths greater than five hydraulic diameters were implemented both upstream and downstream of the valve, a widely adopted criterion to ensure fully developed flow conditions [8].

Pressure measurements were carried out at three points in the system: inlet pressure P_1, pressure at the valve control port P_2, and outlet pressure P_3. The test bench configuration and the location of the measurement points are shown in Figure 2.

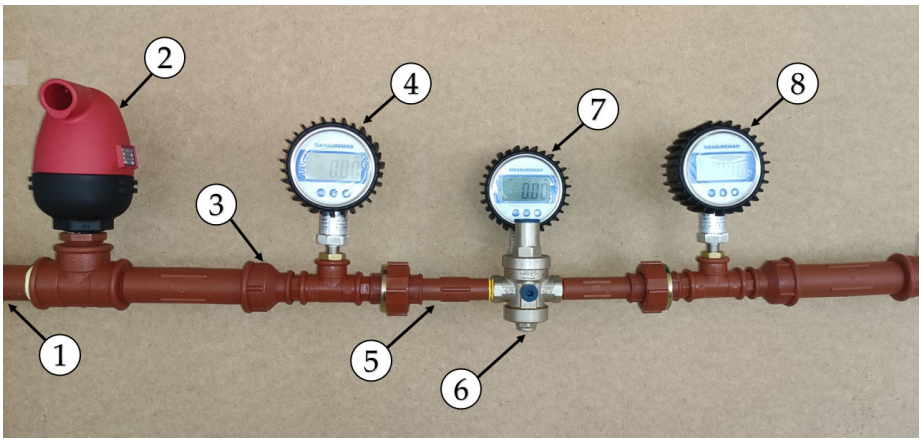

Figure 2. Experimental test bench layout for the characterization of pressure-reducing valves (PRV).

The test bench includes the following main components:

1. 1-inch pipe in the inlet section.
2. Triple-effect air release valve to prevent air accumulation in the system.
3. Reduction from 1″ to 1/2″ to match the pipe with the valve nominal diameter.
4. Inlet pressure gauge (M_1) for measuring inlet pressure (P_1).
5. 1/2-inch pipe upstream of the valve.
6. Pressure-reducing valve under test (DN15).
7. Pressure gauge at the control port (M_2), installed at the threaded connection of the valve, for measuring pressure (P_2).
8. Outlet pressure gauge (M_3) for measuring outlet pressure (P_3).

The air release valve is manufactured by Bermad (Evron, Israel), while the digital pressure gauges, with an accuracy class of 0.5%, are from Measureman (Levallois-Perret, France). Additionally, an ultrasonic flowmeter (VTSYIQI, model TS-2 TM-1, Shenzhen, China) was used for flow measurement, along with a 1-inch gate valve at the outlet to control the flow rate in the system.

2.4. Experimental Procedure and Valve Regulation

In order to ensure comparability between experimental results, numerical simulations, and manufacturer data, the tests were conducted under equivalent conditions by establishing a constant inlet pressure of 8 bar (P_1) and adjusting the valve until reaching the set pressure P_s = 3 bar under static conditions (Q = 0).

It is important to distinguish that P_s corresponds to the set pressure defined by the regulation mechanism, whereas P_1, P_2, and P_3 represent the pressures measured at the inlet, control port, and outlet, respectively.

Valve adjustment was performed under static conditions by regulating the adjustment screw until the desired set pressure was achieved. Subsequently, the flow was enabled through a gate valve to evaluate the valve behavior under dynamic conditions.

Pressure values at points P_1, P_2, and P_3 were recorded for different flow-rate conditions. This allowed for the determination of the pressure drop and the hydraulic characterization of the device within the analyzed flow range.

2.5. CFD Analysis Procedure

The three-dimensional model, shown in Figure 3, was built based on the real dimensions of the valve, reproducing the internal features relevant to its hydraulic behavior. Geometric simplifications were applied, such as the removal of threads and external details that do not influence the internal flow, in order to reduce computational cost without affecting result accuracy [13].

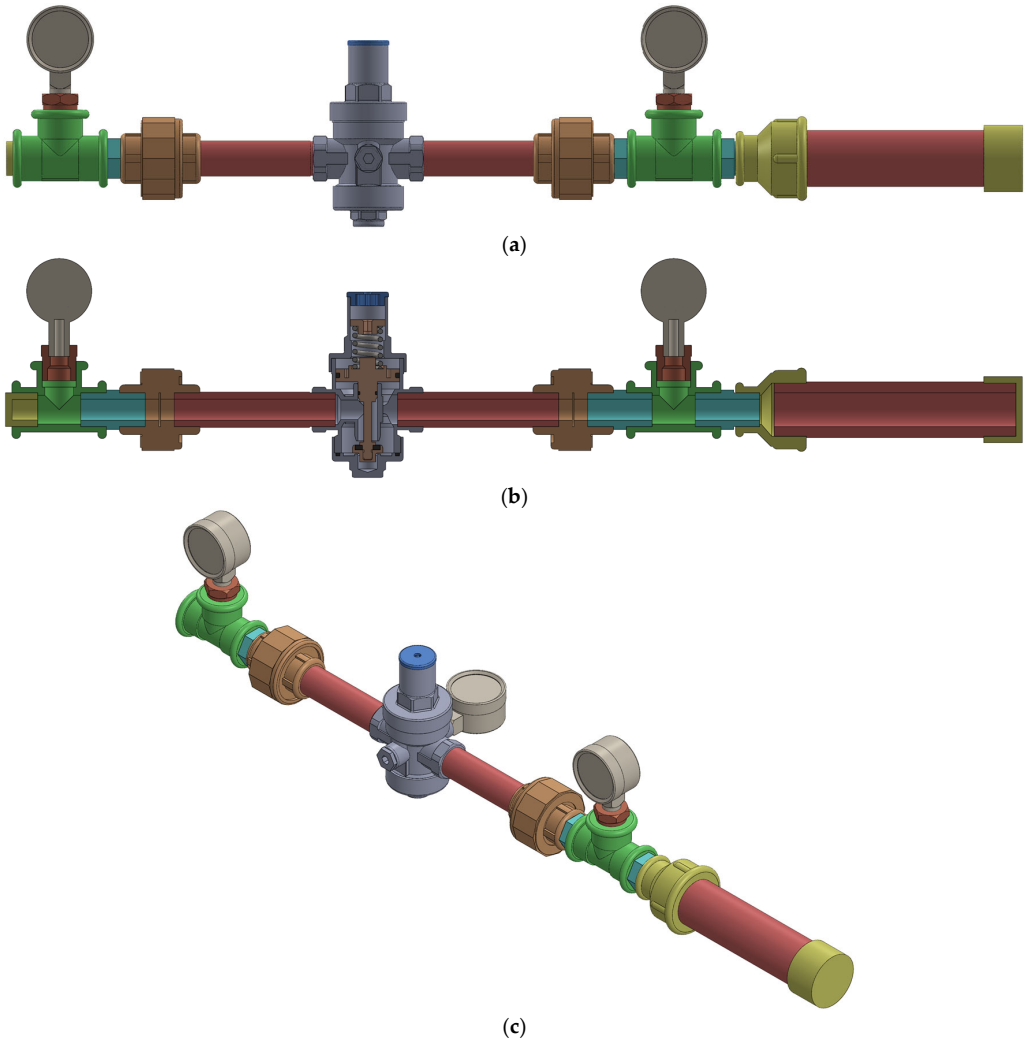

Figure 3. Computational domain: (**a**) complete model, (**b**) sectional view, (**c**) isometric view.

The problem involves a fluid–mechanical coupling due to the spring–piston system, meaning that the outlet pressure does not depend solely on hydraulic restriction but also on the internal force balance. In this context, a sequential approach based on steady-state CFD simulations was adopted to determine the equilibrium operating condition of the valve under different flow rates.

Although the problem may initially be interpreted as a classical fluid mechanics case focused on determining pressure drop in a valve, the pressure-reducing valve (PRV) introduces additional complexity due to its internal regulation mechanism. This mechanism generates a fluid–mechanical coupling between the flow and the spring–piston system, such that the outlet pressure is determined by the balance of internal forces. Consequently, the determination of pressure drop is not a purely hydraulic problem but depends on the interaction between the flow and the regulation system, requiring a rigorous definition of boundary conditions.

The analysis was carried out in two stages:

1. Initial condition (valve closed, $Q = 0$): pressure boundary conditions were imposed at the inlet and outlet, allowing for the determination of the initial hydraulic force acting on the piston F_{H0}.
2. Dynamic regime simulation: simulations were performed for different flow rates (up to 4.5 m^3/h) and valve-lift positions (0–2.6 mm), where the valve lift (s) represents the axial displacement of the piston relative to the fully closed position. For each operating condition, pressures P_1, P_2, and P_3, as well as the hydraulic force F_H, were calculated.

The valve behavior was determined through the balance between hydraulic and spring restoring forces, identifying the equilibrium valve opening for each flow condition. This approach significantly reduces computational cost and is consistent with methodologies used in CFD analysis of valves [14–16].

The force balance methodology was based on the equilibrium between the hydraulic force exerted by the fluid on the piston and the spring restoring force. For each valve-lift position and flow condition, the resultant hydraulic force acting on the piston was obtained directly from the CFD solution by integrating the pressure distribution over all wetted piston surfaces exposed to the internal fluid domain. Under the analyzed operating conditions, the hydraulic force was dominated by pressure effects, while viscous shear contributions were considered negligible. The equilibrium condition was established by assuming that the total hydraulic force must be balanced by the spring restoring force, such that the operating valve opening for each flow condition was determined when:

$$F_H = F_R \tag{4}$$

where F_H represents the resultant force generated by the pressure field on the piston and F_R corresponds to the spring restoring force, obtained from Hooke's law:

$$F_R = k(x_0 - s) \tag{5}$$

The Reynolds number was calculated in order to characterize the flow regime under the analyzed operating conditions [23]. The evaluation was performed using the mean outlet velocity and the hydraulic diameter of the outlet pipe section according to the classical Reynolds-number expression:

$$Re = \frac{\rho v D_h}{\mu} \tag{6}$$

where ρ is the fluid density, v is the mean flow velocity, D_h is the hydraulic diameter of the outlet pipe, and μ is the dynamic viscosity of water at 20 °C.

It should be noted that the software uses absolute pressures for force calculations. However, for analysis and presentation of results, gauge pressures were used, ensuring consistency with the experimental measurements.

2.6. Numerical Configuration

The CFD simulations were performed considering water as the working fluid, with properties evaluated at 20 °C, according to standard values reported in the literature [10].

A no-slip boundary condition was applied at the walls, together with a surface roughness of 1.5 µm, a representative value for smooth metallic surfaces used in hydraulic systems, consistent with typical ranges reported in the literature [8,24].

Turbulence closure was achieved using the modified k–ε model implemented in SolidWorks Flow Simulation 2025 (Dassault Systèmes, Vélizy-Villacoublay, France). According

to the software documentation, this formulation incorporates low-Reynolds-number corrections and near-wall damping functions derived from the Lam–Bremhorst approach, allowing for the resolution of near-wall flow behavior without relying exclusively on standard wall functions. This model was selected due to its robustness, numerical stability, and widespread use in engineering-oriented simulations involving internal turbulent flows and hydraulic devices.

Due to the Cartesian automatic meshing strategy implemented in SolidWorks Flow Simulation, explicit prism-layer inflation, boundary-layer growth factor, and direct $y+$ control are not manually accessible to the user in the same manner as in conventional CFD platforms. Near-wall treatment is internally handled by the modified k–ε model using Lam–Bremhorst low-Reynolds-number damping functions, which provide automatic near-wall resolution within the software framework. Consequently, representative $y+$ values and boundary-layer inflation parameters were not directly available and should be considered a limitation of the present numerical approach.

The computational mesh was generated using a Cartesian-based grid with local refinement in regions characterized by strong pressure and velocity gradients, particularly in the valve seat and throttling region. Additional refinement was applied near the moving piston and narrow flow passages in order to improve the resolution of local flow acceleration, pressure recovery, and hydraulic-force prediction. The detailed mesh configuration and refinement parameters are summarized in Table 2.

Table 2. Numerical configuration and boundary conditions used in the CFD simulations.

Category	Parameter	Value/Description
Software	CFD platform	SolidWorks Flow Simulation
	Analysis type	Internal flow
	Flow regime	Laminar and turbulent
	Simulation type	Steady-state
	Turbulence model	Modified k–ε
Fluid	Working fluid	Water
	Density	998 kg/m^3
	Dynamic viscosity	0.001 Pa·s
	Reference temperature	20 °C
Wall conditions	Boundary condition	No-slip
	Surface roughness	1.5 µm (commercial brass)
Mesh	Mesh type	Cartesian-based
	Global refinement level	3
	Minimum gap size	0.1 mm
	Channel refinement level	7
	Advanced refinement level	5
	Curvature tolerance	0.4 rad
	Minimum cell size	0.25 mm
	Approximate cell count	7.3×10^5 to 7.4×10^5 cells
Monitored variables	Pressures	P_1, P_2, P_3
	Hydraulic force on piston	F_H
	Outlet flow velocity	v

The monitored variables included pressures P_1, P_2, and P_3, outlet flow velocity and the hydraulic force acting on the piston. Convergence of the solutions was verified based on the stability of these variables and the mass balance within the computational domain.

The simulation parameters and boundary conditions are summarized in Table 2, while Figure 4 shows the mesh details in the valve region.

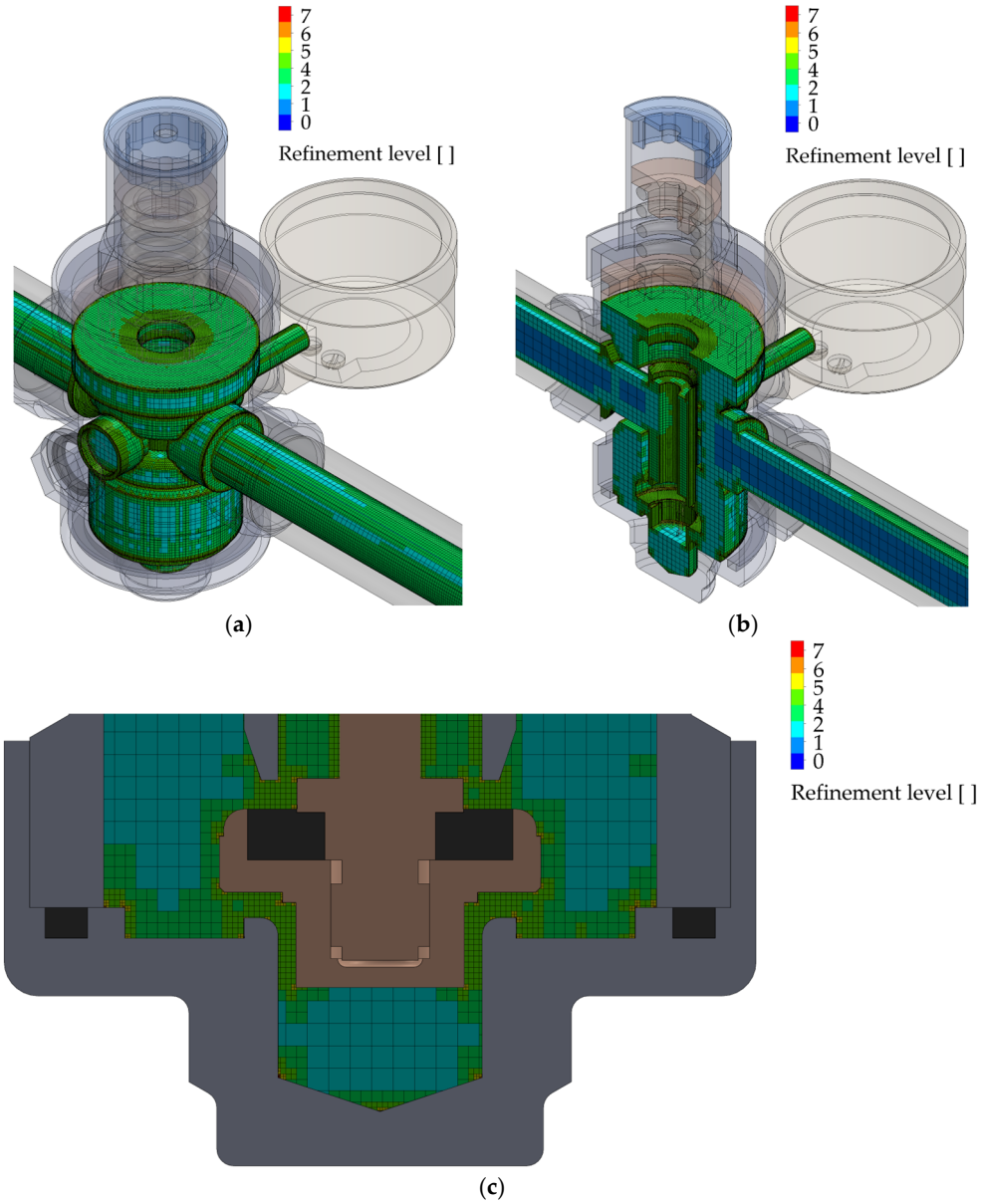

Figure 4. Computational mesh used in the CFD simulations: (**a**) full view of the computational domain, (**b**) sectional view, (**c**) detailed view of the local refinement in the throttling region.

Convergence was assessed by monitoring inlet and outlet pressures, as well as inlet and outlet flow rates, verifying their stability and agreement with the imposed boundary conditions. Mass conservation within the computational domain was also verified.

The variation in the total number of cells between simulations is attributed to changes in the domain geometry associated with valve opening, which affects local mesh refinement in the throttling region. This variation is inherent to the use of automatic mesh generation adapted to geometry.

2.7. Mesh Independence Study

A mesh independence study was performed to evaluate the sensitivity of the numerical results to grid resolution and to ensure that the predicted hydraulic behavior of the valve

was not significantly affected by discretization effects. The analysis was carried out using four progressively refined meshes: coarse, medium, fine, and very fine.

This study was conducted for a representative operating condition corresponding to Q = 3.0 m^3/h and s = 1.7 mm. This condition was selected because it corresponds to an intermediate-to-high flow regime, where strong pressure gradients, local flow acceleration, and hydraulic-force variations occur in the throttling region.

The evaluated variables included control-port pressure (P_2), outlet pressure (P_3), and hydraulic force on the piston (F_H), as these quantities directly govern the hydraulic behavior and force balance equilibrium of the valve. Outlet velocity was not used as an independent grid-convergence indicator because the flow rate was imposed as a boundary condition and the velocity is therefore mainly determined by the outlet cross-sectional area.

For all mesh levels, local refinement was maintained in the valve seat and throttling region, while the global mesh density was progressively increased. Particular attention was given to the narrow flow passages and to the vicinity of the moving piston, where strong velocity gradients and localized pressure variations are expected. This strategy allowed the influence of mesh resolution on the effective flow area, pressure field, and hydraulic-force prediction to be assessed.

All simulations were performed on a Dell Precision workstation equipped with 32 GB RAM and an Intel Xeon Silver processor. Computational runtimes depended on mesh density and operating condition. For the selected fine mesh, the simulation required approximately 90 min to achieve convergence under the analyzed conditions.

3. Results

3.1. Experimental Results

Table 3 presents the experimentally obtained results for a constant inlet pressure of 8 bar and a regulation pressure set to 3 bar under static conditions. As the flow rate increases, the pressures measured at the control port (P_2) and downstream of the valve (P_3) progressively decrease. This behavior reflects the increase in hydraulic losses associated with the operating regime of the pressure-reducing valve.

Table 3. Experimental results for P_1 = 8 bar and set pressure P_s = 3 bar.

Q (m^3/h)	P_2 (bar)	P_3 (bar)	$\Delta P_2 = P_s - P_2$ (bar)	$\Delta P_3 = P_s - P_3$ (bar)	K_v (m^3/h·bar$^{-1/2}$)
0	3	3	0	0	-
0.5	2.96	2.94	0.04	0.06	2.23
1.0	2.90	2.85	0.10	0.15	2.58
1.5	2.81	2.70	0.19	0.30	2.74
2.0	2.68	2.47	0.32	0.53	2.74
2.5	2.48	2.15	0.52	0.85	2.71
3.0	2.25	1.79	0.75	1.21	2.72
3.5	2.05	1.47	0.95	1.53	2.83
4.0	1.89	1.17	1.11	1.83	2.95

During the tests, the inlet pressure (P_1) remained practically constant; therefore, the variations observed in P_2 and P_3 can be directly attributed to the hydraulic behavior of the device. Furthermore, the difference between these two pressures increases with flow rate. While the values of P_2 and P_3 remain relatively similar at low flow rates, at higher flow rates, the downstream pressure becomes significantly lower.

The pressure-drop parameter ΔP_2 was calculated using the pressure P_2 measured at manometer M_2, located at the valve control port. Similarly, ΔP_3 was determined using the outlet pressure P_3 measured at manometer M_3 downstream of the valve. This distinction

was introduced to differentiate between the local pressure response in the regulation zone and the global downstream hydraulic behavior of the valve.

These results suggest that the pressure measured at the control port is affected by local flow phenomena in the regulation region, whereas the outlet pressure P_3 more accurately represents the global hydraulic response of the valve. Consequently, the pressure-drop parameter calculated from P_3 constitutes a more representative indicator for evaluating valve performance.

The flow coefficient K_v was determined considering the relative density of water at 20 °C (ρ_r = 0.99823) using the following expression:

$$K_v = Q\sqrt{\frac{\rho_r}{\Delta P_3}} \tag{7}$$

The obtained values show that the flow coefficient K_v remains within a relatively narrow range as the flow rate increases, with values approximately between 2.2 and 3.0. Although this parameter allows for comparison of the hydraulic capacity of the device, the pressure-drop curves provide a more representative description of regulation-performance degradation in residential pressure-reducing valves.

Figure 5 presents the variation in ΔP_2 and ΔP_3 as a function of flow rate for P_1 = 8 bar. A nonlinear increasing trend is observed, consistent with the increase in local hydraulic losses and flow acceleration in the throttling region. The curve obtained from ΔP_3 shows higher pressure-drop values than those calculated from ΔP_2, with the difference becoming more pronounced beyond approximately Q = 2.0 m^3/h. This behavior confirms that the pressure measured at the control port should not be directly interpreted as outlet pressure under flow conditions.

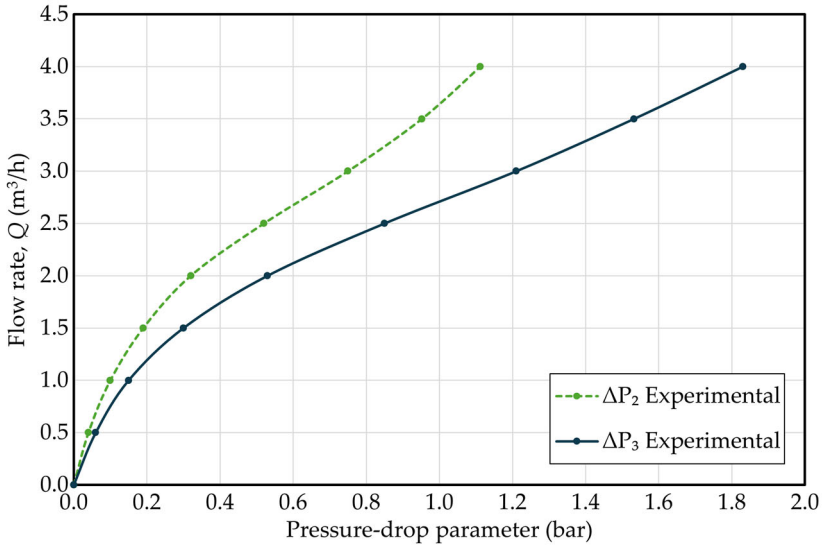

Figure 5. Experimental pressure-drop parameters ΔP_2 and ΔP_3 as a function of flow rate for P_1 = 8 bar.

Experimental uncertainty was mainly associated with the measuring instruments used in the hydraulic test bench. The pressure measurements reported in Table 3 were obtained using digital pressure gauges with an accuracy class of ±0.5% of full scale, while flow-rate measurements were obtained using an ultrasonic flowmeter with an approximate accuracy of ±1% according to manufacturer specifications.

3.2. Mesh Independence Results

Table 4 summarizes the mesh refinement levels, computational times, and monitored hydraulic variables obtained for the representative operating condition corresponding to Q = 3.0 m^3/h and s = 1.7 mm.

Table 4. Results of the mesh independence study for Q = 3.0 m^3/h and s = 1.7 mm.

Mesh Level	Approximate Cell Count	Runtime (min)	F_H (N)	P_2 (bar)	P_3 (bar)
Coarse	4.53×10^5	28.85	354.282	2.861	2.650
Medium	6.92×10^5	56.20	315.927	2.461	2.147
Fine	7.40×10^5	91.93	298.934	2.267	1.851
Very fine	1.07×10^6	126.54	293.685	2.237	1.828

The evaluated variables included the hydraulic force acting on the piston (F_H), the control-port pressure (P_2), and the outlet pressure (P_3), as these quantities directly govern the hydraulic behavior and force balance equilibrium of the valve. Outlet flow velocity was not considered an independent convergence indicator because the flow rate was imposed as a boundary condition and the velocity is therefore mainly determined by the outlet cross-sectional area.

The larger discrepancies observed for the coarse and medium meshes are mainly associated with insufficient resolution of the narrow flow passages in the throttling region. In these cases, the reduced mesh density affects the representation of local pressure gradients and hydraulic-force prediction. As mesh refinement increases, the throttling geometry and pressure field are more accurately resolved, leading to progressive stabilization of the monitored hydraulic variables.

The results show that the relative differences between the fine and very-fine meshes remained below 2% for the hydraulic force and pressure variables, indicating mesh-independent behavior. Although the very-fine mesh provided slightly improved resolution, the associated increase in computational time was significantly higher relative to the observed variation in the monitored variables. Consequently, the fine mesh was selected for the remaining simulations as an adequate compromise between numerical accuracy and computational efficiency.

3.3. Numerical Results for P_1 = 8 bar

The CFD analysis of the initial regulation condition (Q = 0) allowed for determining a hydraulic force acting on the piston of F_{H0} = 381.5N. From this value and the spring stiffness (k = 45.24 N/mm), an initial deformation of x_0 = 8.43 mm was obtained, establishing the relationship between spring restoring force and valve lift.

This initial condition constitutes the starting point for the force balance analysis under different operating regimes. The pressure distribution for this condition is shown in Figure 6, where it is observed that, in the absence of flow, the pressures at the control port and at the outlet are equal.

The spring restoring force as a function of valve lift (s) is given by $F_R = k(x_0 - s)$, with $0 \leq s \leq 2.6$ mm.

Figure 7 shows the hydraulic force curves (F_H) as a function of valve lift for different flow rates, together with the spring restoring force line. The intersection between these curves defines the equilibrium position of the system for each operating condition.

The results indicate that the valve lift increases with flow rate, which is physically consistent, as a larger flow demand requires a greater flow passage area while maintaining regulation capacity. The corresponding equilibrium openings are summarized in Table 5.

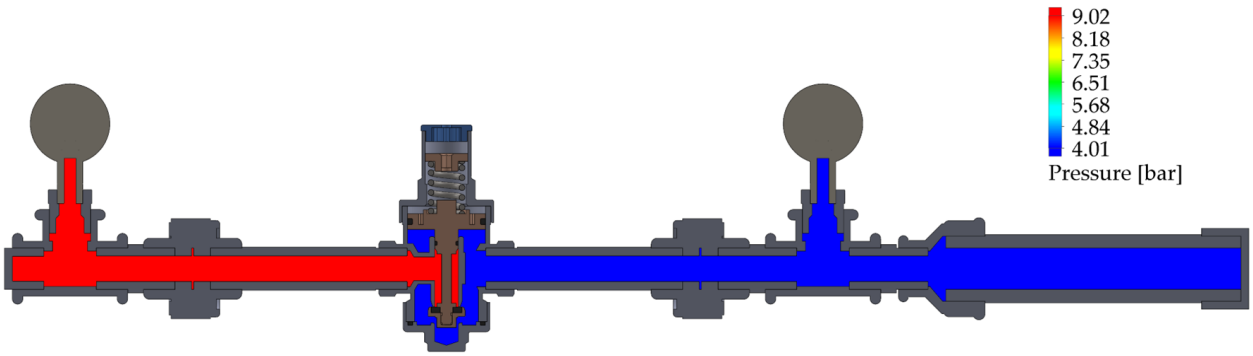

Figure 6. Pressure distribution under closed-valve conditions (Q = 0).

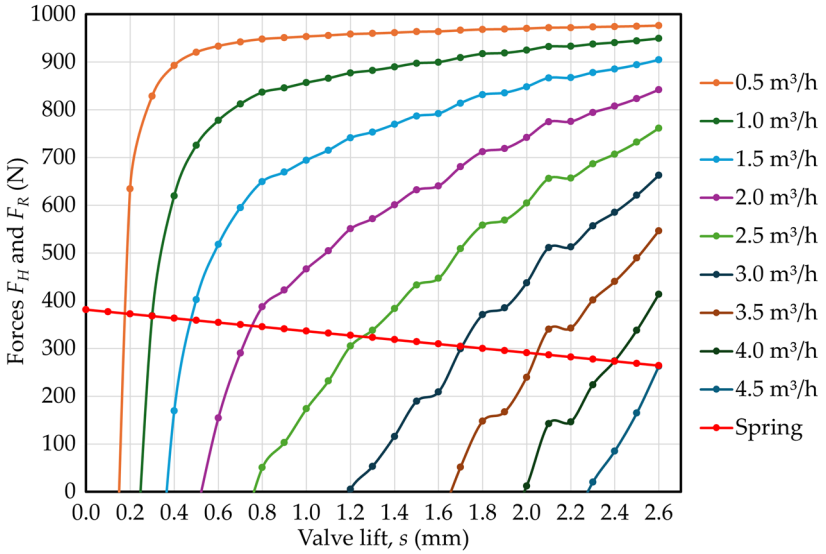

Figure 7. Force balance between hydraulic and spring restoring forces for P_1 = 8 bar.

Table 5. Equilibrium valve lift (s) obtained from the intersection of hydraulic and spring restoring force curves.

Q (m³/h)	s (mm)
0	0
0.5	0.176
1.0	0.300
1.5	0.482
2.0	0.759
2.5	1.259
3.0	1.708
3.5	2.049
4.0	2.398
4.5	2.601

Figure 8 presents the pressure distribution for a representative case (Q = 3.0 m³/h and s = 1.7 mm). It is observed that the highest pressure drop is concentrated in the valve seat region, followed by partial recovery downstream. This behavior is characteristic of throttling-based regulation devices.

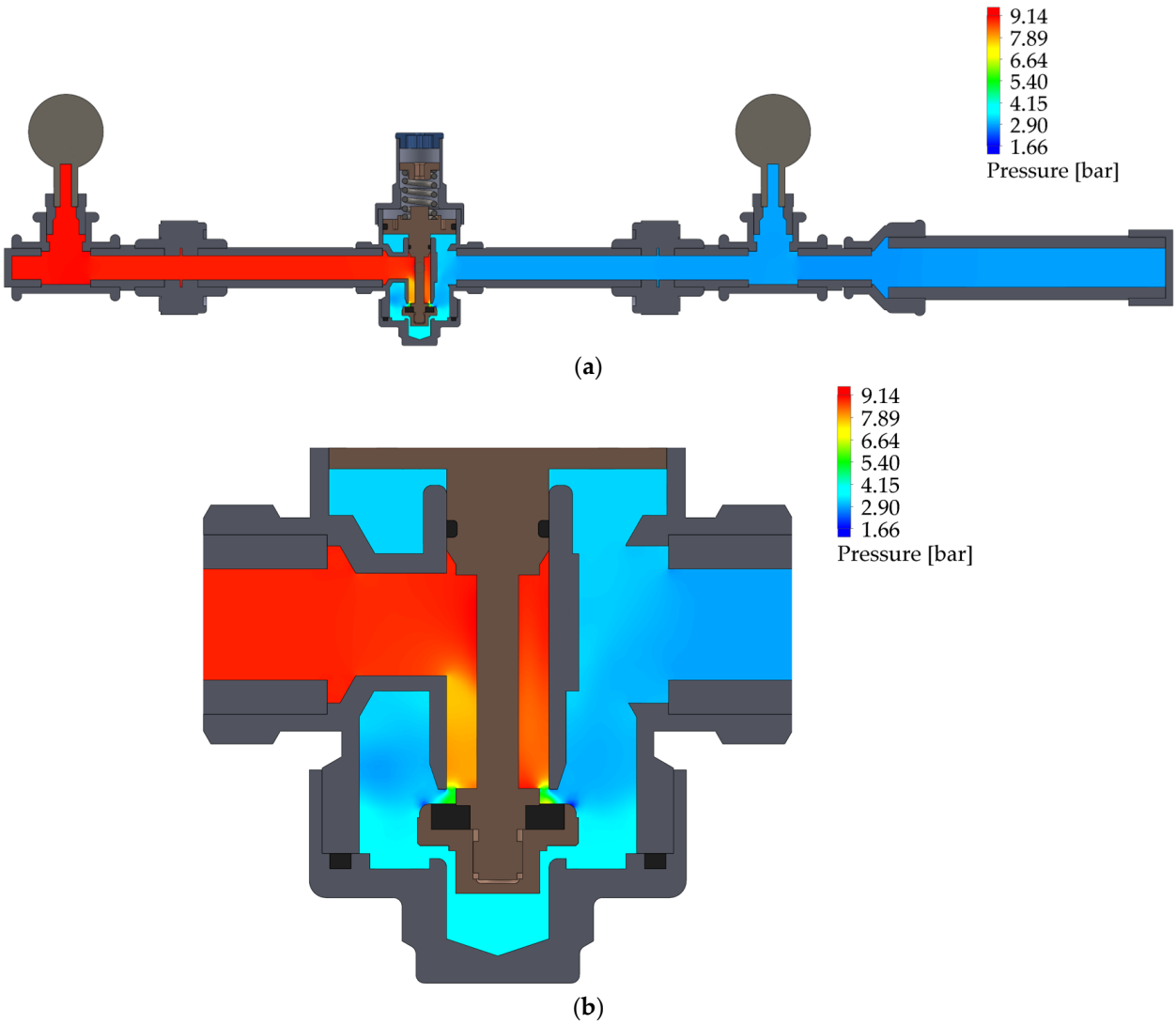

Figure 8. Pressure distribution at Q = 3.0 m^3/h and s = 1.7 mm: (**a**) full model, (**b**) valve detail.

Figure 9 shows the velocity magnitude contours and streamline distribution in the throttling region for the representative operating condition corresponding to Q = 3.0 m^3/h and s = 1.7 mm.

The streamline distribution also reveals vortical structures inside the lateral cavities and downstream chamber of the valve body, indicating the presence of flow separation and recirculation zones generated by the sudden expansion of the flow passage.

The velocity field shows strong local acceleration as the flow passes through the throttling region, where the reduction in effective flow area generates the highest velocities within the valve. The maximum velocities are concentrated near the valve seat due to the formation of localized jets associated with the constricted flow passage.

Downstream of the throttling region, the flow expands into a larger volume, producing regions of velocity reduction and flow recirculation. These flow structures are consistent with the pressure gradients and hydraulic losses observed experimentally and numerically, confirming that the throttling geometry governs the hydraulic response of the valve.

From the equilibrium openings, pressures P_2 and P_3 were determined for each flow rate. The results, presented in Table 6 and Figure 10 show a progressive decrease in both pressures as flow rate increases, maintaining the relationship $P_3 < P_2$. This trend adequately reproduces the experimentally observed behavior.

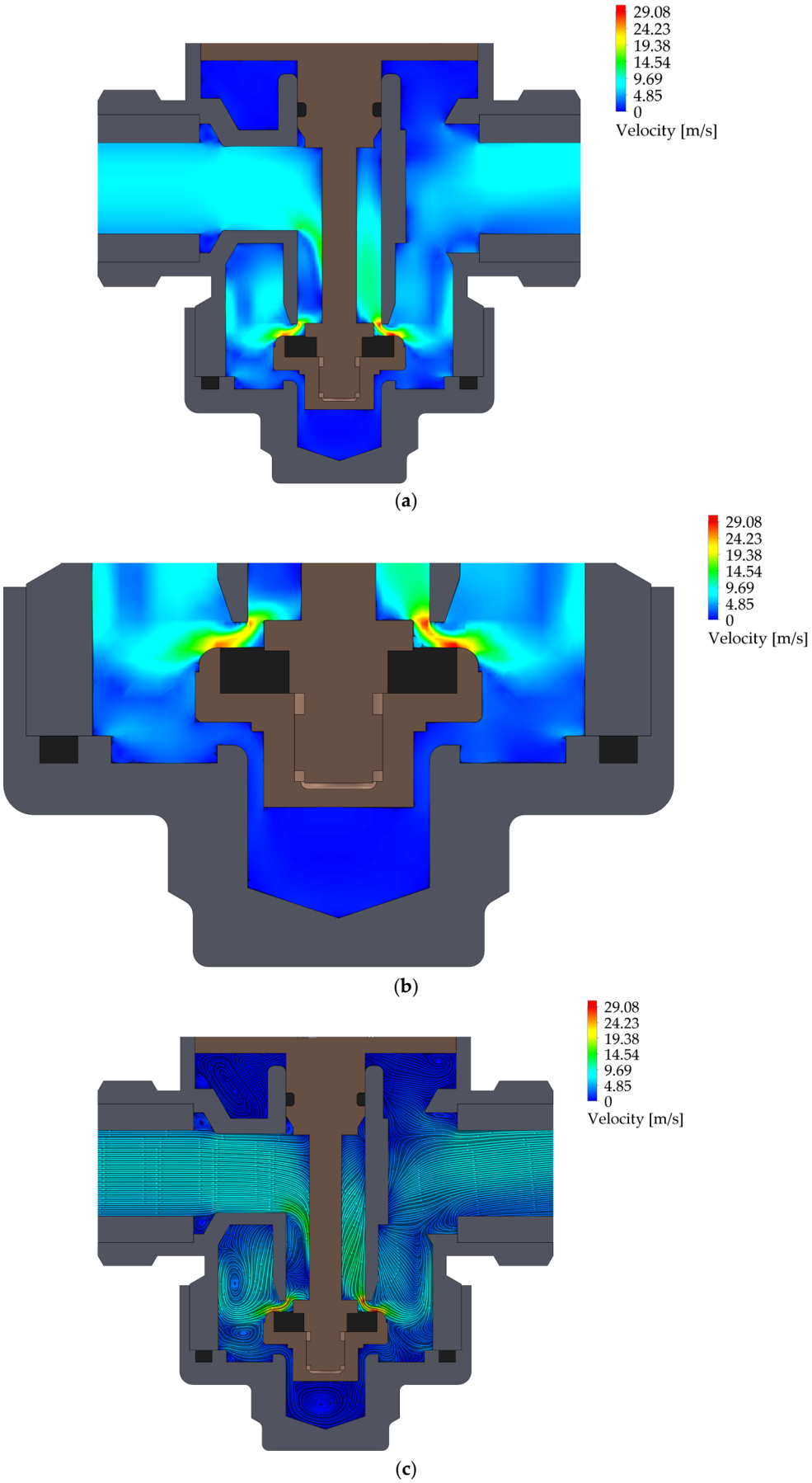

Figure 9. *Cont.*

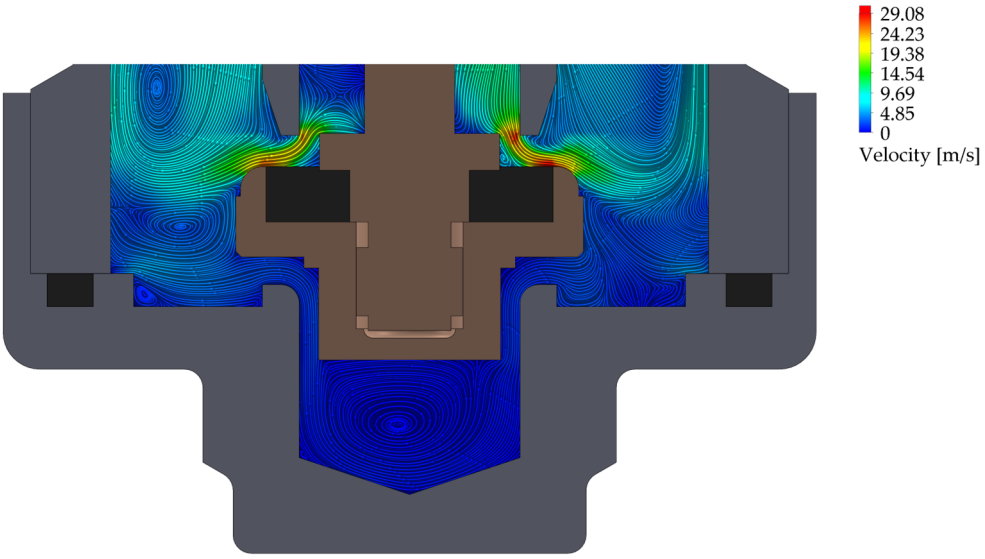

(**d**)

Figure 9. Velocity field and streamlines at Q = 3.0 m^3/h and s = 1.7 mm: (**a**) velocity magnitude contour, (**b**) detailed view of the velocity magnitude contour in the throttling region, (**c**) streamlines, (**d**) detailed view of the streamlines in the throttling region.

Table 6. CFD results for P_1 = 8 bar: pressures, pressure drop, and flow coefficient.

Q (m^3/h)	P_2 (bar)	P_3 (bar)	v (m/s)	Re	$\Delta P_2 = P_s - P_2$ (bar)	$\Delta P_3 = P_s - P_3$ (bar)	K_v (m^3/h·bar$^{-1/2}$)
0	3	3	0	0	0	0	-
0.5	2.97	2.95	0.404	8469	0.03	0.05	2.30
1.0	2.92	2.86	0.809	16,957	0.08	0.14	2.70
1.5	2.83	2.72	1.21	25,391	0.17	0.28	2.81
2.0	2.70	2.50	1.62	33,908	0.30	0.50	2.82
2.5	2.51	2.20	2.02	42,398	0.49	0.80	2.80
3.0	2.31	1.89	2.43	50,908	0.69	1.11	2.85
3.5	2.17	1.59	2.83	59,334	0.83	1.41	2.95
4.0	2.03	1.28	3.24	67,863	0.97	1.72	3.04
4.5	1.82	1.01	3.64	76,223	1.18	1.99	3.19

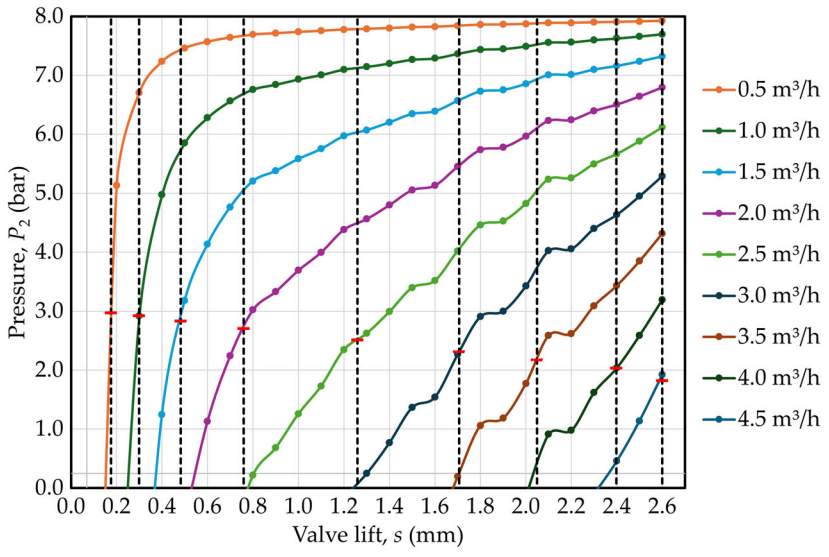

(**a**)

Figure 10. *Cont.*

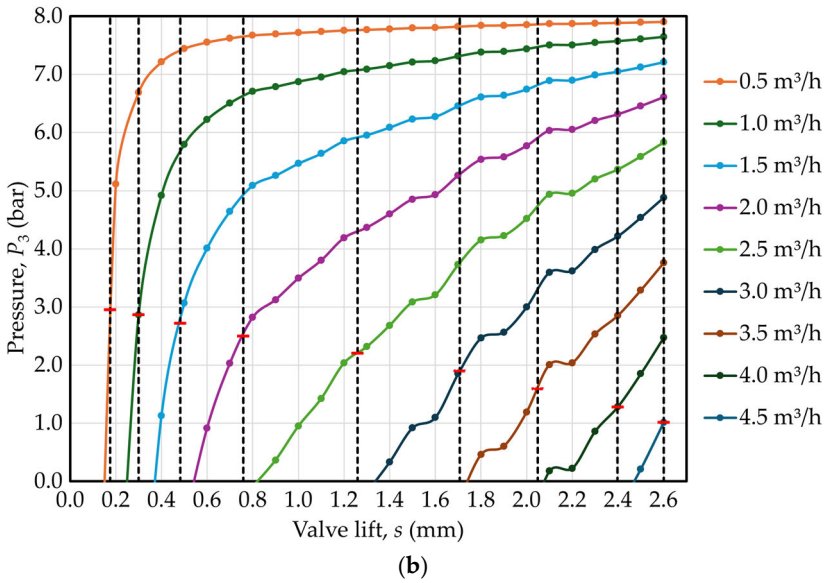

Figure 10. Equilibrium pressures P_2 (**a**) and P_3 (**b**) as a function of valve lift for P_1 = 8 bar. The vertical dashed lines indicate the equilibrium valve-lift positions obtained from Figure 7.

The Reynolds number was calculated using the mean outlet velocity and the hydraulic diameter of the outlet pipe section (D_h = 0.021 m).

Figure 11 shows the pressure-drop curve obtained from CFD, exhibiting a nonlinear trend similar to the experimental results. In particular, the slope of the curve increases at higher flow rates, indicating a progressive reduction in the valve's regulation capacity.

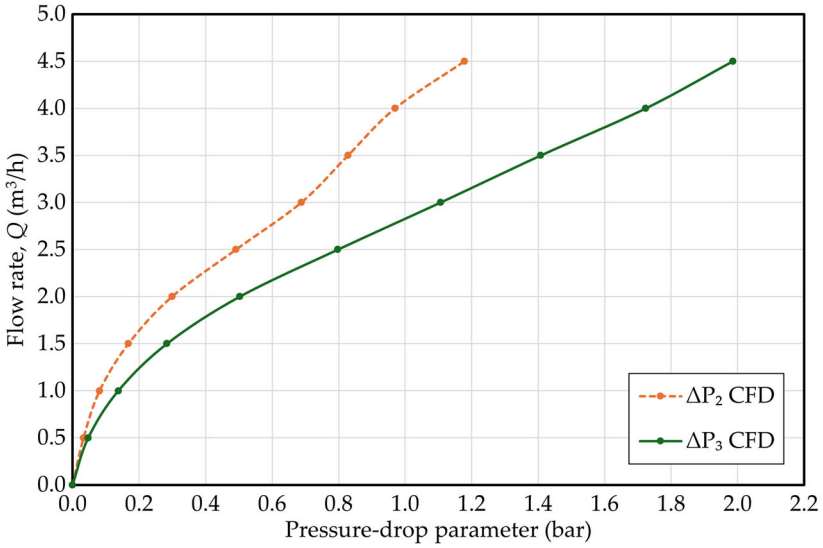

Figure 11. CFD pressure-drop parameters ΔP_2 and ΔP_3 as a function of flow rate for P_1 = 8 bar.

3.4. Comparison Between Experimental and CFD Results

The comparison between experimental and numerical results is presented in Table 7. In general, good agreement is observed between both datasets, with relatively low errors across most of the flow-rate range.

Discrepancies tend to increase at higher flow rates, particularly in the outlet pressure (P_3), where the maximum error remains below 10%. This behavior is consistent with the increasing complexity of the flow under these conditions, characterized by higher turbulence levels, recirculation zones, and sensitivity to numerical discretization.

Table 7. Comparison between experimental and CFD results with relative error for P_1 = 8 bar.

Q (m^3/h)	Experimental P_2 (bar)	CFD P_2 (bar)	Error (%)	Experimental P_3 (bar)	CFD P_3 (bar)	Error (%)
0	3	3	0	3	3	0
0.5	2.96	2.97	0.338	2.94	2.95	0.340
1.0	2.90	2.92	0.690	2.85	2.86	0.351
1.5	2.81	2.83	0.71	2.70	2.72	0.741
2.0	2.68	2.70	0.75	2.47	2.50	1.22
2.5	2.48	2.51	1.21	2.15	2.20	2.33
3.0	2.25	2.31	2.67	1.79	1.89	5.59
3.5	2.05	2.17	5.85	1.47	1.59	8.16
4.0	1.89	2.03	7.41	1.17	1.28	9.40
4.5	-	1.82	-	-	1.01	-

Figure 12 shows the superposition of experimental and numerical pressure-drop curves. A satisfactory agreement is observed at low and intermediate flow rates, while differences increase toward the upper limit of the analyzed range. Despite this, the CFD model adequately reproduces the overall system trends, supporting the validity of the proposed methodology.

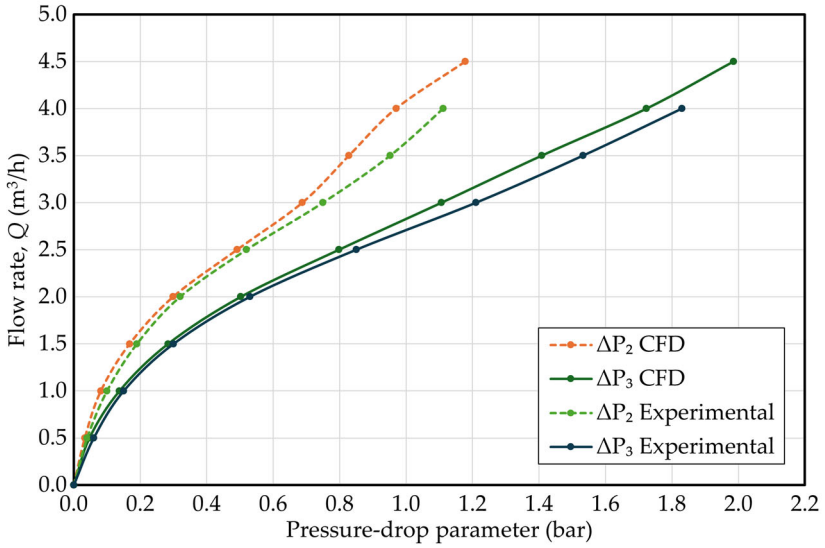

Figure 12. Comparison of experimental and CFD pressure-drop curves for P_1 = 8 bar.

It should be noted that the maximum experimentally tested flow rate was 4.0 m^3/h, whereas simulations were extended up to 4.5 m^3/h. Therefore, the comparison is limited to the common operating range.

3.5. Numerical Results for P_1 = 25 bar and Comparison with Manufacturer Data

Since the manufacturer's curve extends to higher flow rates and pressure drops than those experimentally observed at P_1 = 8 bar, a second set of numerical simulations was performed by imposing an inlet pressure of 25 bar, corresponding to the nominal design pressure of the valve. Figure 13 shows the new force balance under this condition, while Table 8 summarizes the resulting equilibrium valve openings. For the same flow rate, the required openings are smaller than those obtained at 8 bar, indicating that increasing inlet pressure raises the hydraulic force acting on the piston and shifts the equilibrium toward more closed valve positions.

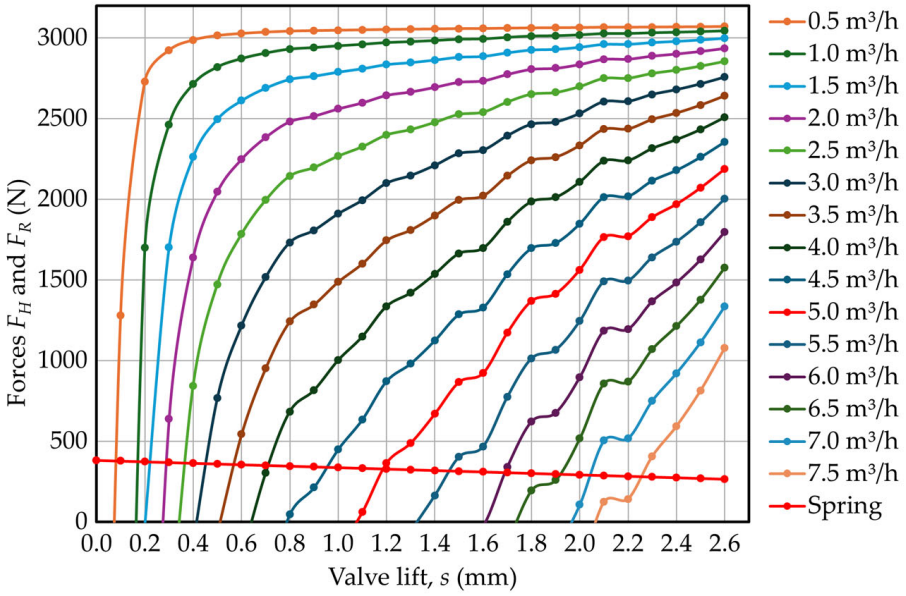

Figure 13. Force balance for P_1 = 25 bar.

Table 8. Equilibrium valve lift (s) for P_1 = 25 bar.

Q (m³/h)	s (mm)
0	0
0.5	0.082
1.0	0.177
1.5	0.222
2.0	0.291
2.5	0.370
3.0	0.455
3.5	0.569
4.0	0.712
4.5	0.954
5.0	1.188
5.5	1.464
6.0	1.691
6.5	1.914
7.0	2.046
7.5	2.252

The interpolated pressures P_2 and P_3 for P_1 = 25 bar are presented in Table 9 and Figure 14. The results show that the downstream pressure decreases significantly as flow rate increases, reaching negative gauge values at high flow rates. This suggests that, under the extreme conditions imposed in the simulation, the valve operates outside its functional regulation range, and pressure recovery becomes insufficient to maintain positive downstream pressures. These values should be interpreted with caution, as they correspond to a numerical extrapolation not experimentally validated.

Figure 15 shows the CFD pressure-drop curves for P_1 = 25 bar, evidencing a substantial increase in ΔP_3 at higher flow rates. When these predictions are compared with the manufacturer's curve in Figure 16, it is observed that the trend obtained at 25 bar more closely matches the catalog data than that obtained at 8 bar, particularly when using P_3.

Table 9. CFD results for P_1 = 25 bar: pressures, pressure drop, and flow coefficient.

Q (m³/h)	P_2 (bar)	P_3 (bar)	v (m/s)	Re	$\Delta P_2 = P_s - P_2$ (bar)	$\Delta P_3 = P_s - P_3$ (bar)	K_v (m³/h·bar$^{-1/2}$)
0	3	3	0	0	0	0	-
0.5	2.98	2.96	0.404	8456	0.02	0.04	2.63
1.0	2.93	2.88	0.808	16,939	0.07	0.12	2.84
1.5	2.84	2.72	1.21	25,428	0.16	0.28	2.81
2.0	2.69	2.49	1.62	33,895	0.31	0.51	2.79
2.5	2.57	2.26	2.02	42,354	0.43	0.74	2.90
3.0	2.50	2.05	2.42	50,760	0.50	0.95	3.08
3.5	2.46	1.85	2.83	59,282	0.54	1.15	3.26
4.0	2.36	1.54	3.23	67,785	0.64	1.46	3.31
4.5	2.24	1.26	3.66	76,681	0.76	1.74	3.40
5.0	2.10	0.93	4.04	84,761	0.90	2.07	3.47
5.5	1.98	0.51	4.44	93,142	1.02	2.49	3.49
6.0	1.82	0.13	4.85	101,736	1.18	2.87	3.54
6.5	1.75	−0.20	5.26	110,251	1.25	3.20	3.63
7.0	1.61	−0.64	5.67	118,735	1.39	3.64	3.67
7.5	1.46	−1.05	6.07	127,143	1.54	4.05	3.72

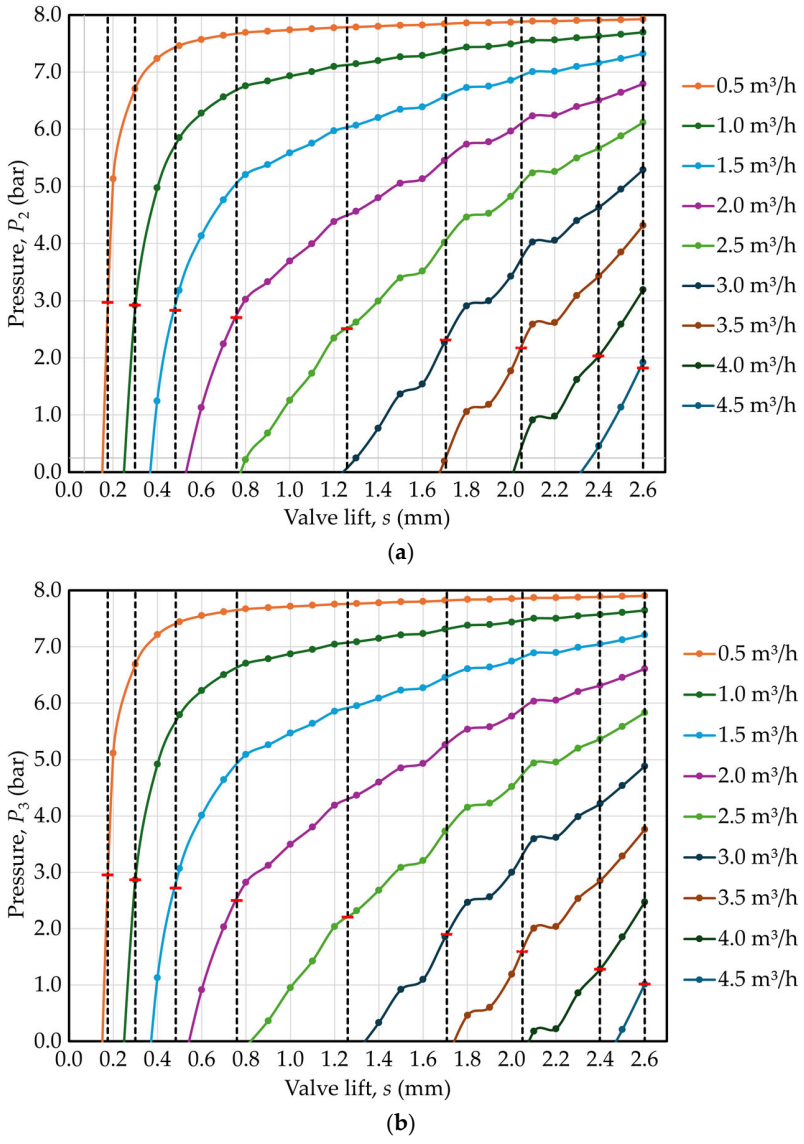

Figure 14. Equilibrium pressures P_2 (**a**) and P_3 (**b**) as a function of valve lift for P_1 = 25 bar. The vertical dashed lines indicate the equilibrium valve-lift positions obtained from Figure 13.

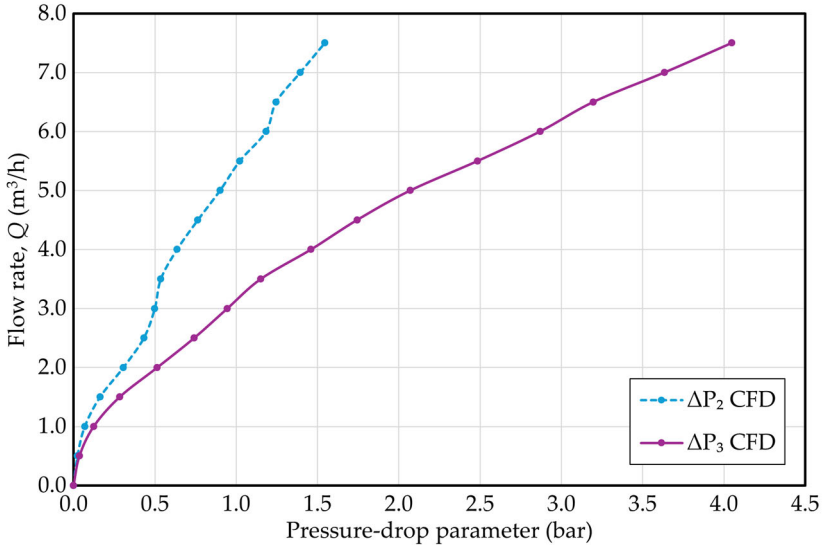

Figure 15. CFD pressure-drop parameters ΔP_2 and ΔP_3 for P_1 = 25 bar.

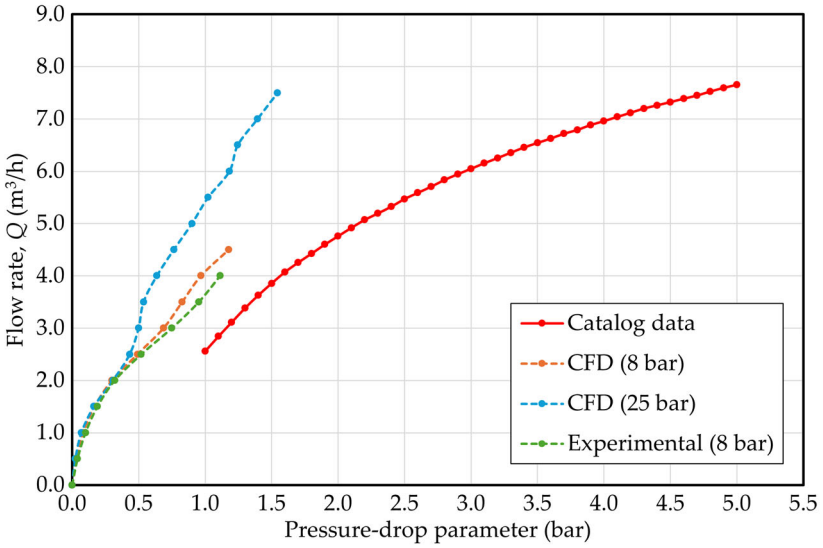

(**a**)

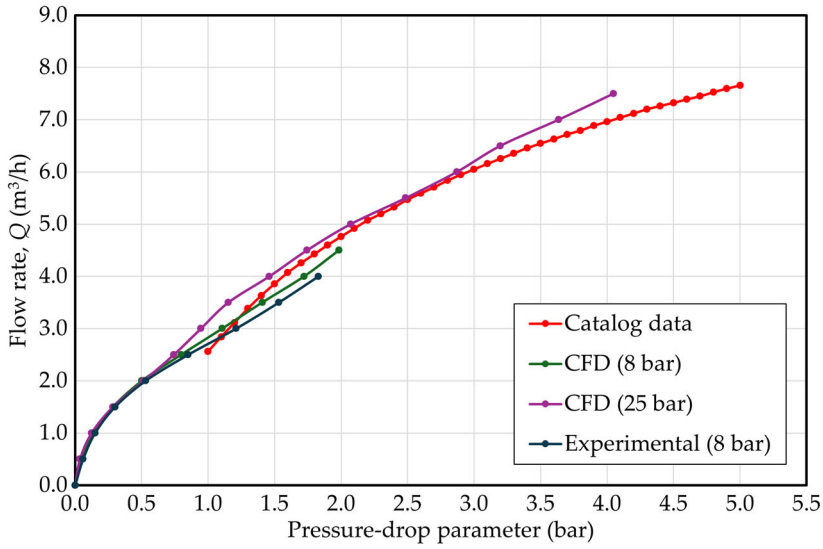

(**b**)

Figure 16. Relationship between flow rate and pressure-drop parameter for experimental results, CFD predictions, and manufacturer catalog data: (**a**) ΔP_2, (**b**) ΔP_3.

This result supports the hypothesis that the manufacturer's curve may have been constructed under conditions closer to the nominal design pressure of the valve rather than typical residential operating conditions. However, this interpretation should be considered a reasonable inference rather than a definitive conclusion due to the lack of experimental validation at high pressure.

3.6. Pressure Regulation Coefficient

Based on the numerical results obtained for 8 and 25 bar, the pressure regulation coefficient S was determined, as summarized in Table 10. This parameter is defined in the performance standard for pressure-reducing valves EN 1567 [1].

Table 10. Pressure regulation coefficient (S) for different flow rates.

Q (m^3/h)	P_3 at P_1 = 8 bar (bar)	P_3 at P_1 = 25 bar (bar)	S
0	3	3	0.000
0.5	2.95	2.96	0.001
1.0	2.86	2.88	0.001
1.5	2.72	2.72	0.000
2.0	2.50	2.49	0.001
2.5	2.20	2.26	0.003
3.0	1.89	2.05	0.009
3.5	1.59	1.85	0.015
4.0	1.28	1.54	0.015
4.5	1.01	1.26	0.014

According to EN 1567, the pressure regulation coefficient S is a dimensionless parameter and therefore should not be interpreted as a percentage.

The pressure regulation coefficient is defined as follows:

$$S = \left| \frac{\Delta P_{out}}{\Delta P_{in}} \right| \tag{8}$$

For example, for Q = 4.5 m^3/h:

$$S = \left| \frac{P_3 \text{ at } P_1 = 25 \text{ bar} - P_3 \text{ at } P_1 = 8 \text{ bar}}{25 - 8} \right| = \left| \frac{1.26 - 1.01}{17} \right| = 0.0142$$

The calculated values of S remain below 0.05 throughout the analyzed flow range, indicating an adequate capacity of the valve to damp variations in inlet pressure.

Although the coefficient S increases with flow rate, its maximum values remain low, on the order of 0.015. This indicates that the device maintains an acceptable regulation response even as demand increases; however, the increasing trend of S also shows that the stability of the outlet pressure progressively deteriorates as the operational limit is approached. In terms of hydraulic performance, this confirms that the valve is suitable within its typical operating range, but its regulation margin decreases noticeably at high flow rates.

4. Discussion

The obtained results show that the proposed methodology, based on steady-state CFD simulations coupled with a sequential force balance procedure, allows for a consistent reproduction of the hydraulic behavior of a direct-acting pressure-reducing valve within the analyzed flow range. The good agreement observed between experimental and numerical results suggests that the hydraulic behavior of the valve can be adequately reproduced

using a steady-state CFD methodology coupled with a sequential force balance procedure, provided that the equilibrium position of the obturator is properly determined from the balance between hydraulic and spring restoring forces.

The monitored variables exhibited progressive stabilization as mesh density increased. The relative differences between the fine and very-fine meshes remained below 2% for hydraulic force and pressure variables, indicating that the numerical solution became effectively independent of further mesh refinement.

Although the very-fine mesh provided slightly improved resolution, the associated computational cost increased considerably. Therefore, the fine mesh was selected for the remaining simulations as an adequate compromise between numerical accuracy and computational efficiency.

The primary objective of the CFD model was not the detailed resolution of transient turbulent structures, but rather the accurate prediction of the pressure distribution and hydraulic force acting on the piston required for the sequential force balance methodology. In this context, the modified k–ε model implemented in SolidWorks Flow Simulation provided stable convergence and satisfactory agreement with the experimental results.

A particularly relevant aspect is the systematic difference between the pressures measured at the control port (P_2) and at the valve outlet (P_3). As the flow rate increases, P_3 decreases more rapidly than P_2, leading to an increasing discrepancy between both magnitudes. This behavior indicates that the pressure at the control port is influenced by local flow phenomena in the regulation zone, whereas the downstream pressure more accurately reflects the global hydraulic response of the system. In this sense, the use of P_3 as a reference variable is more appropriate for evaluating pressure drop and the functional performance of the valve.

From a hydraulic analysis perspective, pressure drop should not be interpreted solely as the difference between inlet and outlet pressures, but rather as the deviation of downstream pressure with respect to the set pressure P_s. In this context, the expression $\Delta P_3 = P_s - P_3$ allows for direct quantification of the degradation of regulation capacity under dynamic conditions, in agreement with the criterion used in manufacturer characterization. This interpretation is particularly relevant for pressure-reducing valves, where the outlet pressure is determined by an internal mechanical equilibrium rather than exclusively by hydraulic losses.

The quantitative comparison between experimental results and numerical predictions shows satisfactory agreement over most of the operating range, with relatively low errors at low and intermediate flow rates. However, discrepancies increase at higher flow rates, which is consistent with the increased flow complexity under these conditions. In particular, enhanced turbulence, the presence of recirculation zones, and greater sensitivity of the pressure field to mesh discretization contribute to the observed differences between both approaches.

The force-balance-based analysis also provides a clear physical interpretation of valve operation. The obturator opening is determined by the intersection between hydraulic and spring restoring force, enabling identification of the operating condition for each flow rate without explicitly modeling the transient behavior of the system. This result reinforces the idea that regulation behavior can be described as a sequence of steady states, simplifying the numerical analysis without significantly compromising predictive capability.

Regarding manufacturer data, the results suggest that the test conditions used to generate catalog curves do not fully coincide with those evaluated experimentally. Although the manufacturer specifies an inlet pressure of 8 bar and a set pressure of 3 bar, the extent of the pressure-drop curve motivated additional simulations at 25 bar. These simulations exhibit a trend closer to the catalog curve, especially when considering downstream pressure (P_3). However, this agreement should be interpreted with caution, as no experimental validation

is available under high-pressure conditions, and therefore conclusions in this regard should be considered indicative rather than definitive.

It should be noted that the negative gauge pressures predicted at high flow rates for P_1 = 25 bar are a consequence of the extreme pressure-drop conditions imposed in the simulations while maintaining a set pressure of P_s = 3 bar. These results indicate a strong reduction in downstream pressure associated with the large hydraulic losses generated in the throttling region. In practical applications, pressure-reducing valves are commonly regulated to higher outlet pressures under high-inlet-pressure conditions, which would reduce the magnitude of the predicted pressure drop. Therefore, the obtained results should be interpreted as a numerical extension of the analyzed operating conditions rather than as typical operating behavior. This also suggests that the manufacturer curve may have been generated under different regulation conditions or through extrapolation at high flow rates.

Finally, the pressure regulation coefficient S remains below 0.05 across the entire analyzed flow range, indicating an adequate capacity of the system to damp inlet pressure variations. However, its progressive increase with flow rate reveals a reduction in regulation efficiency as the valve approaches its operational limit. This behavior is consistent with the increase in pressure drop and the reduction in outlet pressure, confirming that while the device performs adequately within its typical operating range, its regulation capability becomes compromised under high-demand conditions.

The proposed methodology is intended for hydraulic characterization under equilibrium operating conditions and does not attempt to reproduce transient valve dynamics or unsteady turbulent structures that may occur during rapid flow variations.

5. Conclusions

This study enabled the hydraulic characterization of a direct-acting pressure-reducing valve through a combined experimental–numerical approach. Based on the results obtained, the following conclusions are established:

- The methodology based on steady-state CFD simulations, coupled with a force balance analysis, allowed for reproducing the hydraulic behavior of the valve with good accuracy, obtaining a maximum error below 10% in the outlet pressure (P_3) within the analyzed flow range.
- A satisfactory agreement was observed between experimental and numerical results, particularly at low and intermediate flow rates ($Q \leq 3.0$ m^3/h), where discrepancies remain small. At higher flow rates, deviations increase due to the greater complexity of the flow.
- The downstream pressure (P_3) proved to be the most representative parameter for evaluating the global pressure drop, showing higher pressure-drop values than those obtained using P_2, especially for flow rates above 2.0 m^3/h.
- The pressure drop defined as $\Delta P_3 = P_s - P_3$ exhibited a nonlinear increasing trend with flow rate, reaching values on the order of 1.8 bar at Q = 4.0 m^3/h, reflecting the progressive degradation of regulation capacity.
- The force balance analysis allowed for determining valve lift values in the range of 0 to 2.6 mm, increasing with flow rate, confirming the direct relationship between hydraulic demand and effective flow area.
- The flow coefficient K_v remained within a relatively stable range, with values approximately between 2.2 and 3.0, indicating consistent hydraulic behavior of the device within the operating range.
- The pressure regulation coefficient S remained below 0.05 throughout the analyzed range, with maximum values on the order of 0.015, confirming an adequate capacity to damp inlet pressure variations.

- Simulations performed at P_1 = 25 bar showed a better approximation to the manufacturer's curve, suggesting that catalog conditions may be associated with pressures close to the nominal design pressure. However, this interpretation requires additional experimental validation.
- Overall, the valve exhibits adequate performance within its typical operating range ($Q \leq 3.0$ m^3/h), whereas at higher flow rates, a significant increase in pressure drop and a reduction in regulation efficiency are observed.

Author Contributions: Conceptualization, G.L.-V. and P.V.-V.; methodology, G.L.-V. and M.S.-A.; software, G.L.-V.; validation, P.V.-V. and D.P.-Z.; formal analysis, G.L.-V. and S.E.-L.; investigation, G.L.-V. and D.P.-Z.; resources, M.S.-A.; data curation, G.L.-V.; writing—original draft preparation, G.L.-V.; writing—review and editing, P.V.-V., M.S.-A. and S.E.-L.; visualization, D.P.-Z.; supervision, P.V.-V.; project administration, G.L.-V. All authors have read and agreed to the published version of the manuscript.

Funding: This research received no external funding.

Institutional Review Board Statement: Not applicable.

Informed Consent Statement: Not applicable.Please add corresponding content.

Data Availability Statement: The data supporting the results of this study are included in this article. The datasets generated and/or analyzed during this study are available from the corresponding author upon reasonable request.

Acknowledgments: The authors thank the Dirección de Investigación y Desarrollo (DIDE) of the Universidad Técnica de Ambato for supporting this work through the research project PFICM37, "Estudio del comportamiento de válvulas reguladoras de presión en redes domiciliarias y diseño de un nuevo prototipo de mayor eficiencia y seguridad".

Conflicts of Interest: The authors declare no conflicts of interest.

Nomenclature

The following symbols and abbreviations are used in this manuscript:

Q	Volumetric flow rate (m^3/h)
P_1	Inlet pressure (bar)
P_2	Control port pressure (bar)
P_3	Outlet pressure (bar)
P_s	Set pressure (bar)
v	Outlet flow velocity (m/s)
Re	Reynolds number (–)
ΔP_2	Pressure-drop parameter based on control-port pressure (bar)
ΔP_3	Pressure-drop parameter based on downstream outlet pressure (bar)
K_v	Flow coefficient (m^3/h·bar$^{-1/2}$)
S	Pressure regulation coefficient (–)
ρ	Fluid density (kg/m^3)
ρ_r	Relative density (–)
μ	Dynamic viscosity (Pa·s)
F_H	Hydraulic force (N)
F_R	Spring restoring force (N)
k	Spring stiffness (N/mm)
x	Spring displacement (mm)
s	Valve lift (mm)
d	Wire diameter (mm)
D	Mean coil diameter (mm)
D_h	Hydraulic diameter (m)

N	Number of active coils (–)
G	Shear modulus (MPa)
PRV	Pressure-reducing valve
CFD	Computational fluid dynamics

References

1. *EN 1567:1999*; Building Valves—Water Pressure Reducing Valves and Combination Water Pressure Reducing Valves—Requirements and Tests. European Committee for Standardization (CEN): Brussels, Belgium, 1999.
2. Lambert, A. What do we know about pressure: Leakage relationships in distribution systems? In Proceedings of the IWA Conference System Approach to Leakage Control and Water Distribution Systems Management, Brno, Czech Republic, 16–18 May 2001.
3. Rossman, L.A. *EPANET 2.2 User Manual*; U.S. Environmental Protection Agency: Cincinnati, OH, USA, 2020.
4. Prescott, S.L.; Ulanicki, B. Improved control of pressure reducing valves in water distribution networks. *J. Hydraul. Eng.* **2008**, *134*, 56–65. [CrossRef]
5. *ISO 10522:2021*; Agricultural Irrigation Equipment—Direct-Acting Pressure-Regulating Valves. International Organization for Standardization (ISO): Geneva, Switzerland, 2021.
6. Zhang, C.; Li, G. Optimization of a direct-acting pressure regulator for irrigation systems based on CFD simulation and response surface methodology. *Irrig. Sci.* **2017**, *35*, 383–395. [CrossRef]
7. Ferrarese, G.; Malavasi, S. Performances of pressure reducing valves in variable demand conditions: Experimental analysis and new performance parameters. *Water Resour. Manag.* **2022**, *36*, 2639–2652. [CrossRef]
8. Munson, B.R.; Okiishi, T.H.; Huebsch, W.W.; Rothmayer, A.P. *Fundamentals of Fluid Mechanics*, 8th ed.; Wiley: Hoboken, NJ, USA, 2017.
9. Luo, L.; He, X.; Deng, B.; Huang, X. Theoretical and experimental research on a pressure-reducing valve for a water hydraulic vane pump. *J. Press. Vessel Technol.* **2014**, *136*, 021601. [CrossRef]
10. Jin, Z.; Wei, L.; Chen, L.; Qian, J.; Zhang, M. Numerical simulation and structure improvement of double throttling in a high-parameter pressure reducing valve. *J. Zhejiang Univ. Sci. A* **2013**, *14*, 137–146. [CrossRef]
11. Liu, R.; Wang, B.; Wang, R.; Yang, L.; Wang, L.; Ai, C. Improvement of noise reduction structure of direct-acting pressure reducing valve. *Machines* **2024**, *12*, 807. [CrossRef]
12. Xu, E.; Nie, C.; Jiang, X.; Miao, Z. Theoretical investigation on the throttle pressure reducing valve through CFD simulation and validating experiments. *Korean J. Chem. Eng.* **2021**, *38*, 400–405. [CrossRef]
13. Wu, D.; Li, S.; Wu, P. CFD simulation of flow-pressure characteristics of a pressure control valve for automotive fuel supply system. *Energy Convers. Manag.* **2015**, *101*, 658–665. [CrossRef]
14. Wei, L.; Zhu, G.; Qian, J.; Fei, Y.; Jin, Z. Numerical simulation of flow-induced noise in high pressure reducing valve. *PLoS ONE* **2015**, *10*, e0129050. [CrossRef] [PubMed]
15. Talamini Junior, M.V.; de Araujo, A.C.S.; de Camargo, A.P.; Saretta, E.; Frizzone, J.A. Operational characterization of pressure regulating valves. *Sci. World J.* **2018**, *2018*, 1213638. [CrossRef] [PubMed]
16. Ulanicki, B.; Bounds, P.L.M.; Rance, J.P.; Reynolds, L. Open and closed loop pressure control for leakage reduction. *Urban Water* **2000**, *2*, 105–114. [CrossRef]
17. Genebre, S.A. *Redux GE Pressure Reducer Valve with Piston, Art. 3318; Technical Sheet*; Genebre S.A.: Barcelona, Spain, 2025.
18. Saldana, M. The Reynolds Number: A Journey from Its Origin to Modern Applications. *Fluids* **2024**, *9*, 299. [CrossRef]
19. Fagbade, A. Continuous Eddy Simulation vs. Resolution-Imposing Simulation Methods for Turbulent Flows. *Fluids* **2024**, *9*, 22. [CrossRef]
20. Safaei, S.; Mehring, C. Effect of Dissolved Carbon Dioxide on Cavitation in a Circular Orifice. *Fluids* **2024**, *9*, 41. [CrossRef]
21. Genebre, S.A. Redux-GE Pressure Reducing Valve—Product Page. Available online: https://www.genebre.com/redux-ge-piston-pressure-reducer-valve (accessed on 1 April 2026).
22. Budynas, R.G.; Nisbett, J.K. *Shigley's Mechanical Engineering Design*, 11th ed.; McGraw-Hill: New York, NY, USA, 2021.
23. White, F.M.; Xue, H. *Fluid Mechanics*, 9th ed.; McGraw-Hill: New York, NY, USA, 2022.
24. Crane Co. *Flow of Fluids Through Valves, Pipes, Pumps and Fittings*; Technical Paper No. 410; Crane Co.: Stamford, CT, USA, 2022.